



Cite this: DOI: 10.1039/d0cp01992e

First-principles investigation of band offset and charge transfer characteristics at the PE/fluorinated layer interface

Xi Chen, ^a Guangzhi Guo, ^a Yifan Hao, ^a Jiaming Li, ^a Wendong Li, ^a Junbo Deng, ^{*a} Guanjun Zhang, ^{*a} Mingming Zhai, ^b and Wendong Li^a

Polymers, especially polyethylene (PE), are widely employed as insulating materials in electrical power transmission systems. However, the insulation still faces the problem of space charge, which distorts the electric field distribution and accelerates electrical aging. Experimental results show that after the fluorination process, less charge injection occurs compared with pure PE. To clarify the mechanism, classical molecular dynamics was employed to build a PE/fluorinated layer interfacial model and first principles calculation was utilized to get the band offset at the interface. The results calculated by both the bulk plus band lineup method and the layer-decomposed density of states method show that the energy band of the fluorinated PE layer is overall lower than that of the PE side, and the band offsets are around 2 eV. Charge transport results based on Marcus theory and kinetic Monte Carlo simulations also show that charge can easily accumulate at the interfacial area under an electric field and the band offset can suppress charge injection. The conduction band offset acts as an energy barrier for the excess electrons at the fluorinated layer side to cross the interface, while the valence band offset has the same effect on hole transport because of the energy barrier caused by the inverted region. Our findings provide a fundamental and theoretical basis for material modification and space charge inhibition.

Received 13th April 2020,
Accepted 15th July 2020

DOI: 10.1039/d0cp01992e

rsc.li/pccp

I. Introduction

Extruded polymers, especially polyethylene (PE), have been widely used as insulating materials in power transmission cables due to their excellent electrical insulation properties. However, the charge accumulation problems severely limit their application in high voltage direct current cables. It has been revealed that space charge can distort the electric field distribution, causing accelerated degradation and even leading to insulation failure ultimately. To suppress space charge accumulation, extensive studies have been carried out.^{1–4}

It is well known that the space charge in an insulation material is mainly injected through the interface of the polymer insulation and metal electrode from the electrode. Therefore, it is logical to improve the interfacial properties by modifying the polymer surface and thereby suppress charge injection. As one of the most effective surface modifying approaches, fluorination has been widely applied in the chemical industry for not only

fundamental studies but also for industrial applications in the last few decades.⁵ It has been proven that fluorination has a significant suppression effect not only on surface flashover^{6,7} but also on space charge injection.^{8–11} The deeper electron traps, higher dielectric constants and lower free volume are attributed to the obvious charge injection suppression. However, it is still a big challenge to explore the inherent and microcosmic mechanism of the movement of electrons or holes by purely experimental means. Therefore, in this paper, first-principles calculations based on density functional theory (DFT) are mainly utilized to explore the band offset and charge transfer characteristics, both of which have a great influence on the charge movement at the PE/fluorinated layer interface.

Compared with the charge injection process in pure PE, the introduction of the fluorinated layer transforms the original electrode/PE interface into two other interfaces, the electrode/fluorinated layer and PE/fluorinated layer interfaces. Undoubtedly, the charge transfer at the interfaces and within the fluorinated layer differs greatly from the original circumstance. Regarding the electrode/fluorinated layer interface, we have discussed it in ref. 12 with the fluorinated layer represented by a polytetrafluoroethylene (PTFE) oligomer. It was found that compared with PE, the charge transfer at the electrode/PTFE interface results in a more significant vacuum level shift and a higher electron injection barrier.

^a State Key Laboratory of Electrical Insulation and Power Equipment, Xi'an Jiaotong University, Xi'an, 710049, P. R. China. E-mail: dengjb@mail.xjtu.edu.cn, gjzhang@xjtu.edu.cn

^b State Key Laboratory of Fine Chemicals, School of Chemical Engineering, Dalian University of Technology, Dalian, 116024, P. R. China

The higher hole injection barrier might come from the higher ionization energy of PTFE. However, the charge transfer at the PE/fluorinated layer interface is not yet fully understood, which might also have a significant influence on the charge injection. Thus, in this paper, we have calculated the band structure of the interface and simulated the charge transfer using Marcus theory to reveal the charge transfer characteristics at the interface.

This manuscript is organized as follows. In Section II, the methods employed to build the interfacial system model are introduced at first, and then the band offset parameters are computed. In Section III, the basic concepts and parameters of Marcus theory are introduced as well as the computing results. Finally, the main findings are concluded in Section IV.

II. Band offset computation

1. Interfacial system model construction

Previous studies have shown that the fluorination process of PE introduces new functional groups such as $-CF$, $-CF_2$ and $-CF_3$ onto the PE surface.^{5,8} The degree of fluorination depends on the treatment conditions (pressure, temperature and treatment duration), but the fluorination degree inside the fluorinated layer is rather high (sometimes it is close to 90–100%) and the majority of C-H bonds are transformed into C-F bonds.⁵ Although in the fluorination process, the hydrogen atoms in PE cannot be completely displaced by fluorine, to solve the band offset at the interface, the PE/PTFE interface is still utilized to describe the actual interfacial system. For convenience, the fluorinated layer is represented by PTFE in this paper.

Since the crystal lattices of PE and PTFE are not identical and both of them are polymers, the molecular chain distortion at the interfacial area is thus unavoidable. The customary modelling approach used to construct the crystal interfacial geometry, Near-Coincidence-Site Lattice (NCSL) theory,¹³ is difficult to apply in this polymer interfacial system with different lattice types. To properly establish the interfacial model, classical molecular dynamics (MD) is employed in the instruction process.

To simulate the interfacial structures, it is essential to keep the PE and PTFE apart and form a clear boundary. Therefore, suitable construction of the molecular packing in the simulation box is of great importance. The molecule of $C_{40}H_{41}F_{41}$ with a carbon chain is shown in Fig. 1. The carbon chain is composed of two parts with equal numbers of carbon atoms: the PE part with $-CH_2-$ units and the PTFE part with $-CF_2-$ units. This molecule

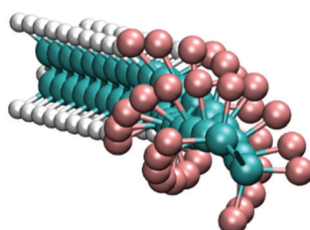


Fig. 1 $C_{40}H_{41}F_{41}$ molecule with a carbon chain packed into the simulation box. The carbon, hydrogen and fluorine atoms are coloured in cyan, white and pink, respectively. The molecule is displayed with VMD.¹⁶

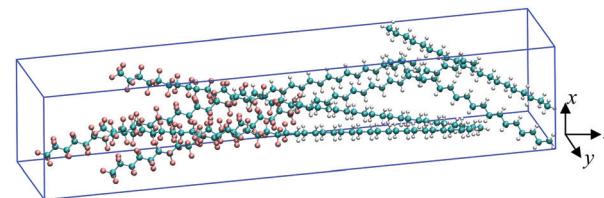


Fig. 2 Initial simulation box packed with six carbon chains. The side lengths are respectively 1.45 nm, 1.45 nm and 7.0 nm in the x, y and z directions.

has been optimized with the Gaussian09 pm6 semi-empirical parameter.¹⁴ The PE part is an all-*trans* structure and the PTFE part is a helix structure. This is in agreement with the reported PTFE structure under atmospheric pressure.¹⁵

After initial optimization, four $C_{40}H_{41}F_{41}$ molecules and another two $C_{20}H_{42}$ molecules are packed into a designed simulation box, as shown in Fig. 2; the side lengths of the box a , b and c are respectively in the x , y and z directions. This process is conducted with Packmol, a structure modelling package.¹⁷ However, since Packmol regards each molecule as rigid and does not support periodic boundary conditions, this model should be further relaxed and compressed into a final model with an actual density. This process is carried out by MD simulations using the Gromacs program.¹⁸

The whole system is initially heated from 0 K to 398.15 K during the first 400 ps and then the temperature is decreased to 298.15 K in the next 200 ps. The final state is then kept for another 2 ns to further relax the structure. The above processes are performed with a V-rescale thermostat and a Berendsen barostat (1 atm) with a time step of 1.0 fs. Three-dimensional periodic boundary conditions are utilized with the all-atom optimized potential for liquid simulations (OPLS-AA) force field. In this simulation, the number of particles, the pressure, and the temperature are kept constant (NPT , 1 atm, 298.15 K) for the last 2 ns to obtain the final structure.

Since the initial packed structure is very loose, when a constant pressure is applied, the structure is compressed and the box shrinks. During this process, the side lengths are fixed in the x and y directions, and only the z direction is shrinkable. After the MD simulation, the structure has a cross-section of $1.45 \text{ nm} \times 1.45 \text{ nm}$ in the x and y directions and a length of 2.93 nm in the z -direction. Vacuum layers are then added on both outside ends along the z -axis and the final size of the simulation box is $1.45 \times 1.45 \times 4.00 \text{ nm}^3$, as shown in Fig. 3.

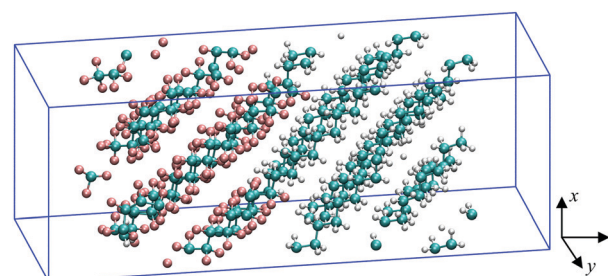


Fig. 3 Final interfacial structure after the MD simulation. The side lengths are respectively 1.45 nm, 1.45 nm and 4.0 nm in the x, y and z directions.

Saiz and Quirke adopted simulation boxes of similar sizes to calculate the bulk and interfacial properties of PE.¹⁹ It has also been proven that a silica slab with a thickness of 1.125 nm was enough to model the band structure in a bulk environment.²⁰ Therefore, our interfacial system is sufficiently large to model the charge transport characteristics at the interface. From Fig. 3, it can be seen that a clear boundary forms between the PE part and the PTFE part, both of which have an equal length along the z-axis. Besides, the carbon chains are parallel to each other, forming a crystal-like structure. After the MD process, the PTFE part also forms an all-trans structure. This is because the force field cannot recognize the helix nature of PTFE. This interfacial system model in the simulation box is composed of 612 atoms. Considering the huge computation, this model is directly utilized as the input structure for first-principles calculations without optimization at the *ab initio* level.

2. Bulk plus band lineup method

The value of band offsets at semiconductor heterojunctions and semiconductor/insulator interfaces greatly influences the charge transport phenomena at these interfaces. A previous study indicated that, as shown in Fig. 4, the valence band offset (Φ_{VBO}) and the conduction band offset (Φ_{CBO}) can be expressed as the following equations:²¹

$$\begin{aligned}\Phi_{\text{VBO}}^{\text{A-B}} &= \mu_{\text{A}} - \mu_{\text{B}} + e\Delta_{\text{ISR}} \\ \Phi_{\text{CBO}}^{\text{A-B}} &= \mu_{\text{A}} - \mu_{\text{B}} + e\Delta_{\text{ISR}} + E_g^{\text{A}} - E_g^{\text{B}}\end{aligned}\quad (1)$$

In the above equations, μ is the energy difference between the valence band maximum (VBM) and the plane averaged electrostatic potential in the bulk environment. Superscript and subscript A/B means insulator A/B. $e\Delta_{\text{ISR}}$ is the difference of the averaged electrostatic potential energies across the interface.

The interfacial parameter, *i.e.* $e\Delta_{\text{ISR}}$, is computed based on the model shown in Fig. 3, while the bulk parameters of PE and PTFE are calculated in the crystal environment shown in Fig. 5. In this study, the experimental lattice constants of PE and PTFE are adopted. PE crystallizes in an orthorhombic cell with lattice

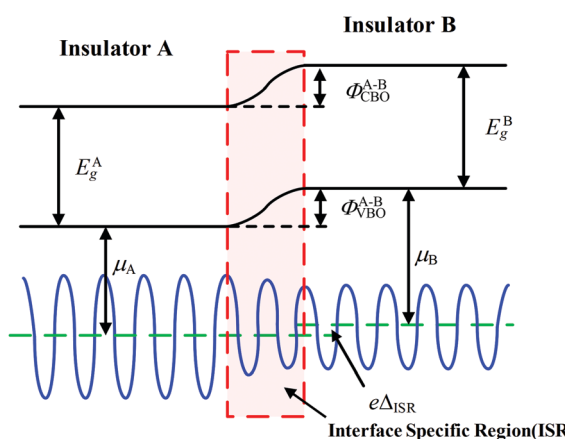


Fig. 4 Band alignment at the insulator A/B interface. $E_g^{\text{A/B}}$ are the band gaps of A/B.

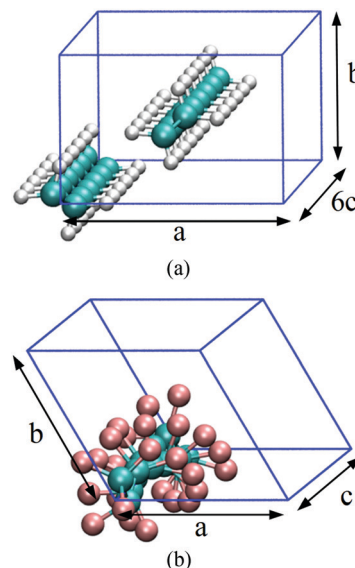


Fig. 5 Crystal lattices of (a) PE and (b) PTFE.

parameters $a = 7.388 \text{ \AA}$, $b = 4.929 \text{ \AA}$, and $c = 2.539 \text{ \AA}$,²² while PTFE has a hexagonal crystal structure. It should be noted that PTFE has 3 phases under atmospheric pressure with changing temperature. The three polymorphs are usually denoted as phase II, stable at temperatures lower than 19°C , phase IV, stable at temperatures between 19 and 30°C , and phase I, stable at temperatures higher than 30°C up to the melting point of 330°C .^{15,23-25} For simplicity, the structure of phase II is adopted as the structure of the fluorinated layer with the crystal parameters of $a = b = 5.59 \text{ \AA}$ and $c = 16.9 \text{ \AA}$.²⁵

After modelling of the above crystal structures and generating the interfacial system using MD, these geometries are then introduced into the Quantum Espresso (PWSCF) code,²⁶ a program based on DFT, to calculate the band structures. The electronic structures are calculated using the generalized gradient approximation (GGA) Perdew–Burke–Ernzerhof (PBE)²⁷ functional exchange–correlation energies and ultrasoft pseudopotentials. The kinetic energy cut-off is set to be 30 Ry for the wavefunctions. Weak interactions, including van der Waals forces, are described by the DFT-D3 functional.²⁸

The plane averaged electrostatic potential along the z-axis is computed according to the following equation

$$\bar{V}(z) = S^{-1} \int_S V(\vec{r}) dxdy \quad (2)$$

where S is the area of the plane perpendicular to the z-direction, and x and y are contained in that plane. $V(\vec{r})$ is the electrostatic datum generated by the PWSCF code. Separate bulk calculations for the PE and PTFE phases are also performed to calculate the difference between the VBM and the electrostatic potential (μ , which is aligned to the interface average electrostatic potential). Besides, the band gaps of PE and PTFE are also calculated to obtain the Φ_{CBO} .

The interface average electrostatic potential is shown in Fig. 6. It can be seen that the electrostatic potential of the PTFE

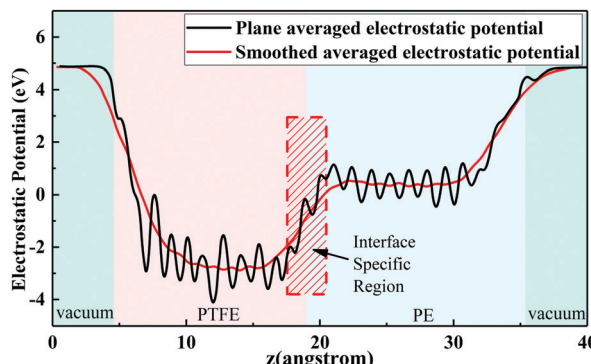


Fig. 6 Average electrostatic potential variation along the z axis of the mixed phase of the PE and PTFE slabs. The black line represents the averaged potential in planes perpendicular to the z axis and the red line represents a smoothed average.

side is overall lower than that of the PE side and the difference is about 3.0 eV. In our study, the bandgaps of PE and PTFE computed from the PBE functional are 6.94 eV and 6.66 eV, respectively. The computed bandgap of PE is very close to the value of 6.9 eV obtained from the VASP code.²⁹ Both of them are significantly lower than the experimental value of 8.8 eV.³⁰ This difference between theoretical (DFT) and experimental values is expected because of the well-known underestimated bandgap of GGA.³¹ In 1990, Seki *et al.* measured the bandgap of PTFE using the vacuum ultraviolet (VUV) adsorption spectrum method, which was found to be about 7.7 eV,^{32,33} while Dake *et al.* measured it to be 6.0 eV using the work function based

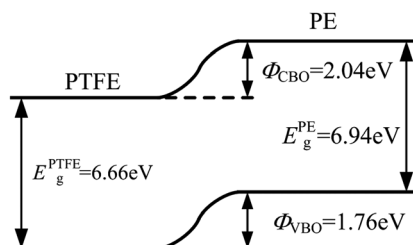


Fig. 7 Schematic representation of the band alignment between PE and PTFE as calculated by the “bulk plus band lineup” method.

method.³⁴ In recent years, with the enhancement of simulation ability, theoretical calculations have become popular. Fatti *et al.* calculated the band gap of the high pressure bulk PTFE and reported it to be 5 eV³⁵ (PBE functional), and Sato *et al.* calculated the band gap of cluster PTFE and found it to be about 8 eV³⁶ (hybrid B3LYP functional). In general, the results achieved by experimental methods and simulation methods are not in good agreement and the calculated band gap of PTFE shows an underestimated trend compared with the experimental results. Since the experiments can be affected by many uncontrollable factors, the simulation results of the band offset can give a theoretical reason for the charge transport at the interface.

The final computed band offset from the “bulk plus band lineup” method is shown in Fig. 7. It can be concluded that both the VBM and the CBM (Conduction Band Minimum) of PTFE are lower than those of PE. The Φ_{VBO} and Φ_{CBO} values are 1.76 eV and 2.04 eV, respectively. This means that the excess electrons prefer to stay at the PTFE side instead of the PE side. The injected electrons in the PTFE side have to pass through the interface with a barrier of about 2.04 eV to enter the PE side. This result gives a good explanation for the experimental phenomenon that the charge injection in fluorinated PE differs greatly from that in the original pure PE.

3. Layer-decomposed density of states (LaDOS) method

To further verify the above result, we have adopted the layer-decomposed density of states (LaDOS) method,³⁷ an effective method proposed by Shi and Ramprasad, to compute the band offset. This method regards the whole system as a composition of several parallel slices. The band offset can be obtained by observing the changing VBM and CBM of each slice along its normal plane. The model shown in Fig. 3 was divided into 8 slices and the projected density of states (PDOS) on each slice was computed. Fig. 8 shows the PDOS of each slice along the z -axis. By connecting the VBM and the CBM of each slice together, the change of the energy band can be clearly observed. As labelled in Fig. 8, Φ_{VBO} is about 1.45 eV and Φ_{CBO} is about 1.88 eV. Although these results are about 0.2–0.3 eV lower than those calculated by the “bulk plus band lineup” method, both the methods show a qualitative agreement that both the VBM and the CBM of PTFE are lower than those of PE.

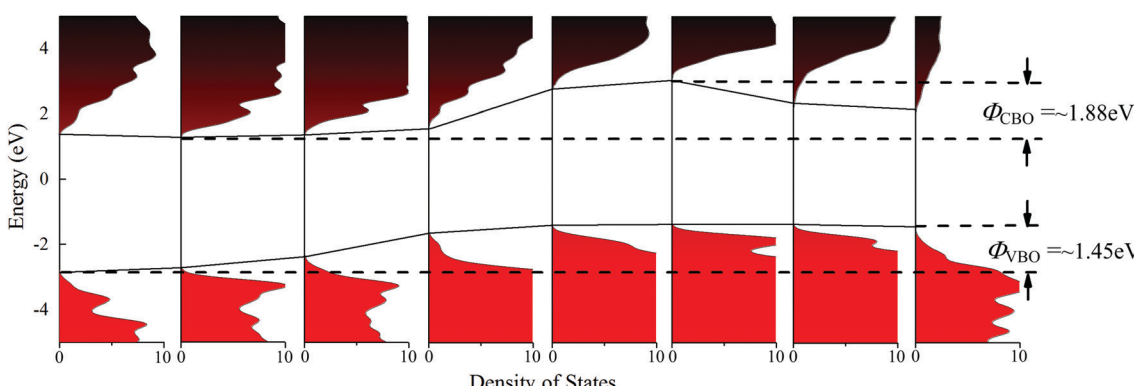


Fig. 8 Schematic representation of the band alignment between PE and PTFE as calculated by the LaDOS method.

Our results strongly indicate that surface fluorination introduces a very high band offset at the interface. These results provide a brand new perspective for us to understand the charge injection phenomena in fluorinated PE. It can be concluded that the band offset plays a key role in the charge injection process. But how it inhibits the charge injection is still unknown since the energy band of PTFE is overall lower than that of PE. In other words, Φ_{CBO} obviously behaves like an energy barrier for excess electrons at the PTFE side but Φ_{VBO} acts like an energy well for the injected holes. For this problem, a more detailed study was further carried out using Marcus theory, as discussed in Section III.

III. Charge transfer at the interface

In recent years, Marcus theory has been utilized to clarify the charge transport in PE. Sato *et al.* successfully applied Marcus theory to determine the mobility of holes in PE with first-principles calculations.^{38–41} In this paper, we apply a similar method to simulate the charge transfer in the vicinity of the interface to reveal the cause of the suppression effect on the charge transport.

The Marcus rate can be calculated according to the following expression,⁴²

$$k_{ij} = \frac{2\pi}{\hbar} \frac{|H_{ij}|^2}{\sqrt{4\pi k_B T \lambda}} \exp \left[-\frac{(\lambda + \Delta G)^2}{4k_B T \lambda} \right] \quad (3)$$

where $|H_{ij}|$ is the electronic coupling between the diabatic initial and final states of φ_i and φ_j , respectively. ΔG is the site energy difference between the initial and final states. λ is the reorganization energy. \hbar , k_B and T are the reduced Planck constant, Boltzmann constant and temperature, respectively.

1. Electronic coupling

Electronic coupling, or the charge transfer integral of the donor and acceptor, is a key characteristic controlling the rate of the charge transfer process. There are several methods to compute this value, including the site-energy correction (SEC) method,⁴³ the fragment charge difference (FCD) method,⁴⁴ and the generalized Mulliken-Hush method.⁴⁵ In this paper, we applied the SEC and the FCD methods to calculate the electronic coupling between the PE and PTFE oligomers. Using the SEC method, the electronic coupling can be expressed as

$$H_{ij} = \frac{J_{ij} - \frac{1}{2}(e_i - e_j)S_{ij}}{1 - S_{ij}^2}$$

$$e_i = \langle \varphi_i | \hat{H} | \varphi_i \rangle$$

$$J_{ij} = \langle \varphi_i | \hat{H} | \varphi_j \rangle \quad (4)$$

φ_i and φ_j are the nonorthogonal initial and final charge localized states used to derive e_i and J_{ij} . S_{ij} is the overlap between φ_i and φ_j .

For the FCD method, electronic coupling is written as

$$J_{ij} = \langle \varphi_i^* | \hat{H} | \varphi_j^* \rangle = \frac{(E_2 - E_1)|\Delta q_{12}|}{\sqrt{(\Delta q_1 - \Delta q_2)^2 + 4\Delta q_{12}^2}}. \quad (5)$$

Here, $E_2 - E_1$ is the energy difference between the orbitals involved (HOMO and HOMO-1 for the hole transfer mechanism⁴⁴ and LUMO and LUMO+1 for the electron transfer mechanism⁴⁶). φ_i^* and φ_j^* are the localized states derived from the adiabatic states ψ_1 and ψ_2 by orthogonal transformation

$$\begin{pmatrix} \varphi_i^* \\ \varphi_j^* \end{pmatrix} = T^{-1} \begin{pmatrix} \psi_1 \\ \psi_2 \end{pmatrix} = \begin{pmatrix} \cos \omega & -\sin \omega \\ \sin \omega & \cos \omega \end{pmatrix}^{-1} \begin{pmatrix} \psi_1 \\ \psi_2 \end{pmatrix} \quad (6)$$

$$\tan \omega = \frac{2|\Delta q_{12}|}{|\Delta q_1 - \Delta q_2|}.$$

Here, Δq_{12} is the transition charge difference. Δq_1 and Δq_2 are the donor-acceptor charge difference for each adiabatic state.

2. Reorganization energy and free energy difference

Reorganization energy is an important parameter in the Marcus charge transfer equation. The reorganization energy is usually composed of an inner-sphere (λ_i) part and an outer-sphere (λ_o) part. λ_i reflects the energy change derived from structural changes of the reacting molecules, while λ_o results from solvent relaxation. In a nonpolarized solvent, λ_o is usually an order of magnitude smaller than λ_i and thus can be neglected. The most commonly used method to calculate λ_i is Nelsen's four-point method,⁴⁷ which is an accurate approximation for inter-molecular charge transfer where the donor and acceptor molecules have nearly no effect on each other.⁴⁸ In this paper, the reorganization energy λ refers to the inter-sphere part λ_i .

Fig. 9 shows the diagram of the reorganization energy calculation during the process of hole (positive charge) transfer.³⁸ The corresponding reorganization energies λ_A and λ_D are also labelled. The diagrams in Fig. 9 illustrate the energy change of the (a) donor and (b) acceptor molecule, respectively. So, the reorganization energy can be expressed as⁴⁹

$$\lambda = \lambda_D + \lambda_A = \{E_{D^+}(Q_D) - E_{D^+}(Q_D^+)\} + \{E_A(Q_A^+) - E_A(Q_A)\}. \quad (7)$$

While the total free energy difference is evaluated through

$$\Delta G^0 = G_D^0 + G_A^0 = \{E_{D^+}(Q_D^+) - E_D(Q_D)\} + \{E_A(Q_A) - E_A(Q_A^+)\} \quad (8)$$

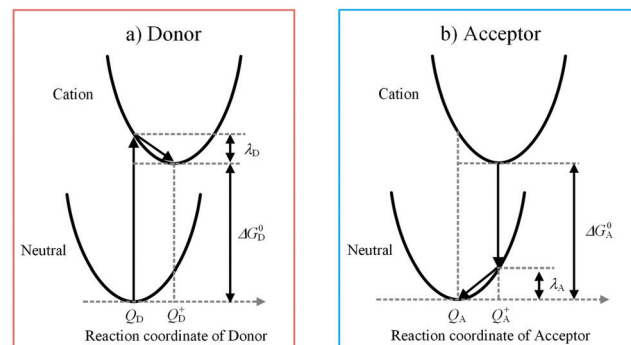


Fig. 9 Schematic diagram of the reorganization energy calculation through a four-point method. The curves show the energy change of (a) the donor and (b) the acceptor molecules during the charge transfer.

Q_D and Q_A represent the equilibrium structures of the neutral donor and acceptor molecules, respectively, and the superscript “+” denotes the cation.

3. Two-dimensional interfacial model construction

It has been proven in a previous study⁴¹ that environmental polarization has little influence on the electronic coupling of PE oligomers. Besides, the amorphous morphology of PE does not change the hopping regime of hole transport.⁴⁹ Since this paper mainly concentrates on the interface problem, a simplified two-dimensional model based on the crystal structure is thus adopted. The two-dimensional interfacial model is constructed with the crystal structures of PE and PTFE, as shown in Fig. 10(a) and (c). For the orthorhombic crystalline structure of PE, according to the crystal constant, the closest distance between each PE chain can be calculated to be about 4.44 Å. The distance between each PTFE chain is exactly the crystal constant, *i.e.* 5.59 Å. Due to the mismatch of the crystal constants across the interface, the molecular arrangement takes a simple form, as shown in Fig. 10(b). In Fig. 10(a)–(c), the arrows represent the charge hopping direction from the central molecule to the next site. It should be noted that, in Fig. 10(a), the inter molecule distance indicated by the red arrow is longer than that indicated by the black arrow. Therefore, the electronic coupling in crystal

PE gives two different values. Fig. 10(d) shows a 3D view of the interfacial model and the corresponding location of the crystal PE, PTFE, and the interfacial area. The PTFE and PE oligomers are chosen to be $C_{13}F_{28}$ and $C_{13}H_{28}$, respectively. This is because one crystal lattice of PTFE (under 19 °C) contains 13 carbon atoms. It should be noted that $C_{13}H_{28}$ shows liquid characteristics at room temperature but our research target is solid PE. Therefore, the conformational change of the oligomer, for example, the rouse motion, and local reptation are not taken into account during the charge transfer process. The length of the PE part along the x -axis is set to be 500 nm.

Since Fig. 10(b) only gives a rough description of the PE/PTFE dimer arrangement, the electronic coupling is exactly calculated according to the optimized dimer configuration shown in Fig. 11. The distance between the monomers and the full geometry of the structure are optimized at the B3LYP-D3 (B3LYP⁵⁰ with Grimme's DFT-D3 correction²⁸) level of theory. This theory has been proven to be able to reasonably calculate the configuration and the interaction energy of some small nonpolar dimers such as $(H_2)_2$, $(N_2)_2$ and $(H_2)(N_2)$, while the pure hybrid functional B3LYP gives the wrong configuration and even a positive interaction energy.⁵¹ In this section, all the DFT calculations were carried out by using the Gaussian09¹⁴ package in conjunction with the 6-31g* basis set.⁵²

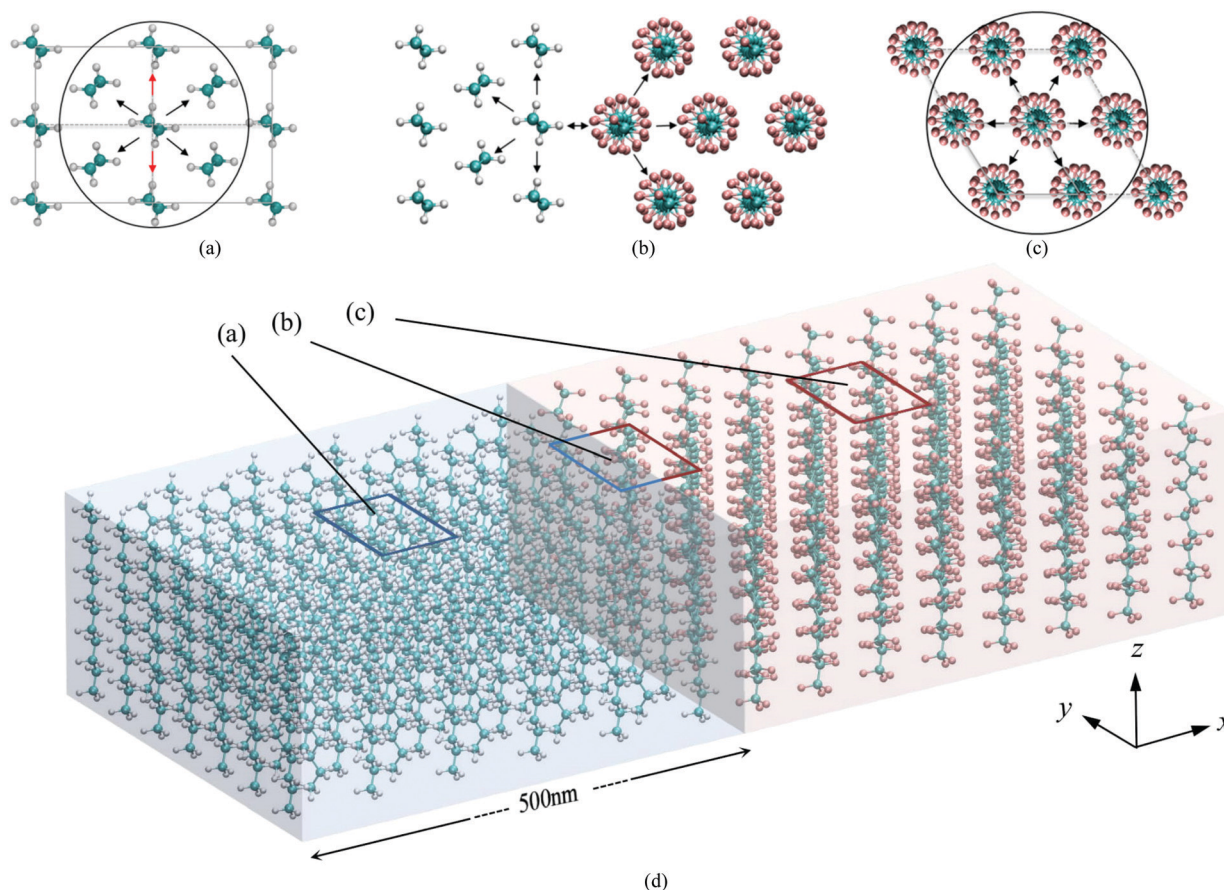


Fig. 10 Structure of the (a) crystal PE, (b) interfacial molecular arrangement, and (c) crystal PTFE and (d) 3D view of the 2D interfacial model and the corresponding area of (a)–(c).

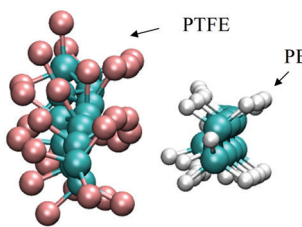


Fig. 11 Optimized configuration of the PTFE/PE oligomer dimer.

4. Calculated results and charge transfer simulation

It has been revealed that the unoccupied orbitals of PE oligomers show Rydberg-like states,⁵³ which means that the excess electron distribution is highly delocalized. These properties are also consistent with the negative electron affinity of PE and the inter-chain states⁵⁴ of excess electrons in the bulk environment, while PTFE has an intra-chain state of excess electrons.⁵⁵ For this reason, quantitative analysis of the electron transfer rate and the electron transfer simulation were not conducted in this paper.

The calculated electronic coupling, free energy difference, and reorganization energy are shown in Table 1. Here, the PE oligomer is considered to be the electron acceptor, while the PTFE oligomer is the electron donor. It can be seen that both the SEC method and the FCD method give similar results of electronic coupling; therefore, the values obtained from the SEC method are adopted for subsequent discussion.

From the Marcus parameters calculated from the HOMOs, it is obvious that the reorganization energy of the PTFE oligomer is smaller than that of the PE oligomer. This is reasonable since the PTFE chain is rigid, while the PE chain is more flexible. When hole hopping occurs, geometry relaxation of the PTFE oligomer therefore occurs to a much lesser extent than that in PE chains. The calculated hole transfer rates are $2.76/0.203 \times 10^7 \text{ s}^{-1}$, $2.55 \times 10^{11} \text{ s}^{-1}$, and $4.95 \times 10^{-25} \text{ s}^{-1}$ for the PE, PTFE, and PE/PTFE dimers, respectively. Compared with the large transfer rate between the PE or the PTFE dimer, hole hopping from PE to PTFE oligomer is nearly impossible. This result is dominated by the large free energy difference (1.65 eV) between the PE and PTFE oligomers. This value is very close to but a

Table 1 Electronic coupling, free energy difference and reorganization energy between the HOMOs and the LUMOs of different dimers

| Dimer | Electronic coupling (H_{ij} , meV) | | Free energy difference (ΔG_0 , eV) | Reorganization energy (λ , eV) |
|------------------------------------------------------------------|------------------------------------------|--------------------|---------------------------------------------------|--------------------------------------------|
| | FCD | SEC | | |
| HOMOs | | | | |
| C ₁₃ H ₂₈ –C ₁₃ H ₂₈ | 2.56/0.68 | 2.64/0.72 | 0.0 | 0.87 |
| C ₁₃ F ₂₈ –C ₁₃ F ₂₈ | 5.45 | 5.55 | 0.0 | 0.17 |
| C ₁₃ H ₂₈ –C ₁₃ F ₂₈ | 5.60 | 5.60 | 1.65 | 0.52 |
| LUMOs | | | | |
| C ₁₃ H ₂₈ –C ₁₃ H ₂₈ | — | — | 0.0 | 0.05 |
| C ₁₃ F ₂₈ –C ₁₃ F ₂₈ | 23.9 | 24.2 | 0.0 | 0.28 |
| C ₁₃ H ₂₈ –C ₁₃ F ₂₈ | — | 208.6 ^a | -2.85 | 0.16 |

^a Due to the delocalized state of the PE oligomer's LUMO distribution, this value is inaccurate and is only adopted for qualitative analysis.

little larger than the calculated Φ_{VBO} for a bulk environment. Even when 1.45 eV (Φ_{VBO} calculated by the LaDOS method) is adopted as the free energy difference, a transfer rate of about $3.63 \times 10^{-20} \text{ s}^{-1}$ can still be neglected.

Due to the delocalized state of PE's conduction band distribution, the electronic coupling of electron transfer cannot be calculated accurately.⁵⁴ Besides, it has been proven that the electronic coupling of electron transfer in PE is extraordinarily large and electron transfer occurs in the band regime instead of the hopping regime.³⁶ Therefore, the discussion of electron transfer in PE based on Marcus theory is inaccurate. The calculated electronic coupling for electron transfer of the C₁₃H₂₈–C₁₃F₂₈ dimer is also larger than the reorganization energy, which goes beyond the hopping regime. Thus, there might be an error in the calculated results. The following is a qualitative discussion instead of a quantitative one. The calculated free energy difference during electron transfer for the PE/PTFE dimer is -2.85 eV, whose absolute value is much larger than Φ_{CBO} calculated in the last section. This may be caused by different calculation environments and functionals (PBE for the bulk model and B3LYP for the isolated dimer). However, this difference does not change the final qualitative results. Because even if we take -1.88 eV (Φ_{CBO} obtained by the LaDOS method) as the free energy difference for an electron moving from the PE side to the PTFE side, since the absolute value is far larger than the reorganization energy, the calculated transfer rate still remains smaller than that calculated in the PE or PTFE bulk environment. Since electronic coupling has little influence on the final charge transfer rate, the inaccurate electronic coupling in Table 1 is simply employed and the electron transfer rate would be $5.14 \times 10^{-63} \text{ s}^{-1}$. According to Marcus theory, this might be caused by the inverted region. The calculated results indicate that a large free energy difference, the absolute value of which is much larger than the reorganization energy, would inhibit both the hole and electron transport, whether the free energy difference is positive or negative.

However, the actual situation is more complex. Holes at the PE side can easily move to the interface driven by the applied electric field and then start to accumulate there. As the accumulation increases, the free energy difference decreases because the HOMO or the VBM is filled with holes and thus the holes start to jump from HOMO-1, HOMO-2 or even lower orbitals.

To simulate the hole transport at the interface, the hole mobility was computed in the presence of an external electric field. The effect of the electric field was evaluated by adding the energy difference

$$\Delta G = \Delta G_0 - eE(r_f - r_i) \quad (9)$$

into eqn (3), where e is the elementary charge, E is the applied electric field and ΔG_0 is the free energy difference computed with no electric field. r_i and r_f denote the initial and final locations of holes during the hole hopping process.

To clearly display the charge transport process at the interface, based on the computed hopping rate using Marcus theory, kinetic Monte Carlo (KMC) simulation was then applied to simulate the hole transport at the interfacial area. This method

has been applied for the evaluation of hole mobility in 2-dimensional PE, and it has been proven to be able to give semi-quantitative hole mobility data compared with experimental results.³⁸ After the calculation of the hopping rates from the initial hopping site m to all its neighbors, the hopping probability for the hole to the n th neighbor is determined as⁵⁶

$$P_{mn} = k_{mn} / \sum_{n'} k_{mn'} \quad (10)$$

Here, n' is the total number of accessible adjacent hopping sites. Since electronic coupling decays exponentially with the distance between hopping sites, a long-distance jump is not taken into consideration. In the PE and PTFE bulk environment, n' is set to be 6 (see Fig. 10(a) and (c)). For the interfacial area, *i.e.* the PE/PTFE dimer, n' is set to be 4 or 5 according to the configuration shown in Fig. 10(b). After the determination of the next hopping site, the KMC simulation time is evaluated as⁵⁶

$$\Delta t = 1 / \sum_{n'} k_{mn'} \quad (11)$$

Under the electric field, the hole mobility is evaluated as

$$\begin{aligned} v &= \mu E \\ vt &= (r(t) - r(0)) \cdot \frac{E}{|E|} \end{aligned} \quad (12)$$

Here, μ is the hole mobility and v is the velocity of the hole.

To compare our results with a previous reported study,³⁸ the starting point of charge transport is set at the PE side. Fig. 12 gives 8 independent trajectories of holes starting to transport from the zero position in the x -direction to the interface under an electric field. It can be seen that the hopping probability of the holes in the PE oligomers passing over the barrier to the PTFE oligomers is very low. This is due to the large free energy difference at the interface. Therefore, under the electric field, most holes accumulate at the interface. Fig. 13 gives the x coordinate and the corresponding time of each hole. With time, the x coordinates of each hole show some difference but most holes stop moving on when the interface is encountered. The corresponding hole mobility was calculated and is illustrated in Fig. 14. At the initial time, the mobility fluctuates within a wide

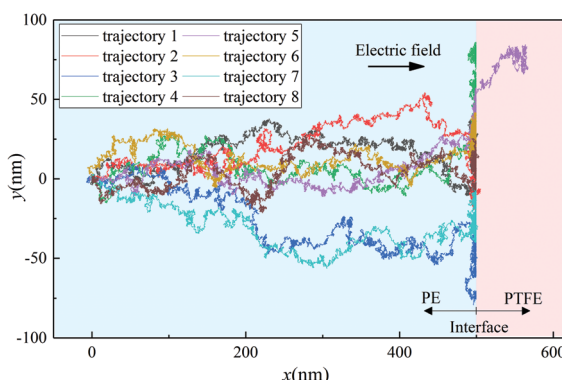


Fig. 12 Eight hole trajectories at the $C_{13}H_{28}/C_{13}F_{28}$ interface from KMC simulations with Marcus theory at 300 K.

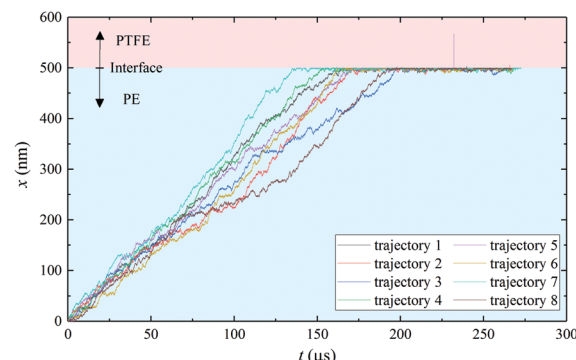


Fig. 13 Relation between time and displacement in the direction of the applied electric field (10 kV mm^{-1} along the x -direction).

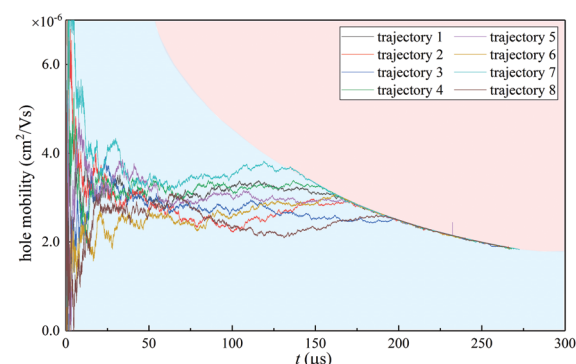


Fig. 14 Time dependent hole mobility along the x axis.

range because of the random movement. Later on, the mobility tends to become steady and the average value is around $3.0 \times 10^{-6} \text{ cm}^2 \text{ V}^{-1} \text{ s}^{-1}$. This value is very close to the result calculated for the $C_{10}H_{22}$ oligomers.³⁸ Finally, nearly all the trajectories reach the mobility limitation of $x_{\text{int}}/|E|t$. Here, x_{int} is the length of the PE part along the x -axis, *i.e.* 500 nm. E is the applied electric field and t is time.

IV. Conclusions

To summarize, we have applied a multiscale approach combining molecular dynamics, first principles and kinetic Monte Carlo simulations to study the suppression effect on charge transport caused by PE fluorination. With the fluorinated layer replaced with PTFE, both the bulk plus band lineup method and the LaDOS method illustrate a band offset around 2 eV at the interface and the energy bands of PTFE are overall lower than those of PE. KMC simulation based on Marcus theory shows that under an electric field, charges can easily accumulate at the interface and the band offset plays a key role in charge transport suppression. Φ_{CBO} at the interface serves as an energy barrier that can significantly suppress electron injection. The negative Φ_{VBO} has the same effect on hole transport due to the existence of an inverted region.

Conflicts of interest

There are no conflicts to declare.

Acknowledgements

We are very thankful to Prof. Guohui Li at the Dalian Institute of Chemical Physics (DICP) and Prof. Jianhua Yang at the Dalian University of Technology (DUT) for their basic specialized guidance and great help. This work was supported by the National Natural Science Foundation of China (NNSFC) (No. 51577150 and U1766218).

Notes and references

- 1 F. Tian, Q. Lei, X. Wang and Y. Wang, *Appl. Phys. Lett.*, 2011, **99**, 142903.
- 2 T. Takada, Y. Hayase, Y. Tanaka and T. Okamoto, *IEEE Trans. Dielectr. Electr. Insul.*, 2008, **15**, 152–160.
- 3 J. Xue, H. Wang, J. Chen, K. Li, Y. Liu, B. Song, J. Deng and G. Zhang, *J. Appl. Phys.*, 2018, **124**, 11.
- 4 J. Xue, Y. Li, J. Dong, J. Chen, W. Li, J. Deng and G. Zhang, *J. Phys. D: Appl. Phys.*, 2020, **53**, 155503.
- 5 A. Kharitonov, *Prog. Org. Coat.*, 2008, **61**, 192–204.
- 6 C. Wang, J. Guo, W.-D. Li, X.-R. Li, Z.-H. Jiang, B.-H. Guo and G.-J. Zhang, *Mater. Lett.*, 2019, **249**, 17–20.
- 7 C. Wang, W.-D. Li, J. Guo, X. Chen, Z.-H. Jiang, X.-R. Li, B.-H. Guo and G.-J. Zhang, *Appl. Surf. Sci.*, 2019, 144432.
- 8 Z. An, Q. Yang, C. Xie, Y. Jiang, F. Zheng and Y. Zhang, *J. Appl. Phys.*, 2009, **105**, 064102.
- 9 Z. An, C. Xie, Y. Jiang, F. Zheng and Y. Zhang, *J. Appl. Phys.*, 2009, **106**, 104112.
- 10 Z. An, C. Liu, X. Chen, F. Zheng and Y. Zhang, *J. Phys. D: Appl. Phys.*, 2011, **45**, 035302.
- 11 J. Xue, J. Chen, J. Dong, G. Sun, J. Deng and G. Zhang, *Int. J. Elec. Power*, 2020, **120**, 105979.
- 12 X. Chen, A. Zhao, J. Li, J. Deng, G. Zhang and X. Zhao, *J. Appl. Phys.*, 2019, **126**, 035101.
- 13 T. Sayle, C. Catlow, D. Sayle, S. Parker and J. Harding, *Philos. Mag. A*, 1993, **68**, 565–573.
- 14 M. J. Frisch, G. W. Trucks, H. B. Schlegel, G. E. Scuseria, M. A. Robb, J. R. Cheeseman, G. Scalmani, V. Barone, B. Mennucci, G. A. Petersson, H. Nakatsuji, M. Caricato, X. Li, H. P. Hratchian, A. F. Izmaylov, J. Bloino, G. Zheng, J. L. Sonnenberg, M. Hada, M. Ehara, K. Toyota, R. Fukuda, J. Hasegawa, M. Ishida, T. Nakajima, Y. Honda, O. Kitao, H. Nakai, T. Vreven, J. A. Montgomery, Jr., J. E. Peralta, F. Ogliaro, M. Bearpark, J. J. Heyd, E. Brothers, K. N. Kudin, V. N. Staroverov, R. Kobayashi, J. Normand, K. Raghavachari, A. Rendell, J. C. Burant, S. S. Iyengar, J. Tomasi, M. Cossi, N. Rega, J. M. Millam, M. Klene, J. E. Knox, J. B. Cross, V. Bakken, C. Adamo, J. Jaramillo, R. Gomperts, R. E. Stratmann, O. Yazyev, A. J. Austin, R. Cammi, C. Pomelli, J. W. Ochterski, R. L. Martin, K. Morokuma, V. G. Zakrzewski, G. A. Voth, P. Salvador, J. J. Dannenberg, S. Dapprich, A. D. Daniels, Ö. Farkas, J. B. Foresman, J. V. Ortiz, J. Cioslowski and D. J. Fox, *Gaussian09, Revision D. 01*, Gaussian Inc., Wallingford, CT, 2009.
- 15 E. S. Clark, *Polymer*, 1999, **40**, 4659–4665.
- 16 W. Humphrey, A. Dalke and K. Schulten, *J. Mol. Graphics*, 1996, **14**, 33–38.
- 17 L. Martínez, R. Andrade, E. G. Birgin and J. M. Martínez, *J. Comput. Chem.*, 2009, **30**, 2157–2164.
- 18 D. Van Der Spoel, E. Lindahl, B. Hess, G. Groenhof, A. E. Mark and H. J. Berendsen, *J. Comput. Chem.*, 2005, **26**, 1701–1718.
- 19 F. Saiz and N. Quirke, *Phys. Chem. Chem. Phys.*, 2018, **20**, 27528–27538.
- 20 T. P. M. Goumans, A. Wander, W. A. Brown and C. R. A. Catlow, *Phys. Chem. Chem. Phys.*, 2007, **9**, 2146–2152.
- 21 R. T. Tung and L. Kronik, *Adv. Theory Simul.*, 2018, **1**, 1700001.
- 22 S. Kavesh and J. Schultz, *J. Polym. Sci., Part A-2*, 1970, **8**, 243–276.
- 23 C. A. Sperati and H. W. Starkweather, *Fortschritte Der Hochpolymeren-Forschung*, Springer, 1961, pp. 465–495.
- 24 E. S. Clark, *J. Macromol. Sci., Part B: Phys.*, 2006, **45**, 201–213.
- 25 E. Clark and L. Muus, *Z. Kristallogr. – Cryst. Mater.*, 1962, **117**, 119–127.
- 26 P. Giannozzi, S. Baroni, N. Bonini, M. Calandra, R. Car, C. Cavazzoni, D. Ceresoli, G. L. Chiarotti, M. Cococcioni, I. Dabo, A. Dal Corso, S. de Gironcoli, S. Fabris, G. Fratesi, R. Gebauer, U. Gerstmann, C. Gougoussis, A. Kokalj, M. Lazzeri, L. Martin-Samos, N. Marzari, F. Mauri, R. Mazzarello, S. Paolini, A. Pasquarello, L. Paulatto, C. Sbraccia, S. Scandolo, G. Scalauzero, A. P. Seitsonen, A. Smogunov, P. Umari and R. M. Wentzcovitch, *J. Phys.: Condens. Matter*, 2009, **21**, 395502.
- 27 J. P. Perdew, K. Burke and M. Ernzerhof, *Phys. Rev. Lett.*, 1996, **77**, 3865.
- 28 S. Grimme, J. Antony, S. Ehrlich and H. Krieg, *J. Chem. Phys.*, 2010, **132**, 154104.
- 29 L. Chen, T. D. Huan and R. Ramprasad, *Sci. Rep.*, 2017, **7**, 1–10.
- 30 K. Less and E. Wilson, *J. Phys. C: Solid State Phys.*, 1973, **6**, 3110.
- 31 A. Huzayyin, S. Boggs and R. Ramprasad, *IEEE Trans. Dielectr. Electr. Insul.*, 2010, **17**, 926–930.
- 32 K. Seki, H. Tanaka, T. Ohta, Y. Aoki, A. Imamura, H. Fujimoto, H. Yamamoto and H. Inokuchi, *Phys. Scr.*, 1990, **41**, 167.
- 33 A. Palov, H. Fujii, Y. Mankelevich, T. Rakimova and M. Baklanov, *Polym. Degrad. Stab.*, 2012, **97**, 802–809.
- 34 S. B. Dake, N. R. Rajopadhye and S. V. Bhoraskar, *J. Phys. D: Appl. Phys.*, 1987, **20**, 1631–1636.
- 35 G. Fatti, M. C. Righi, D. Dini and A. Ciniero, *J. Phys. Chem. C*, 2019, **123**, 6250–6255.
- 36 M. Sato, A. Kumada and K. Hidaka, *IEEE Trans. Dielectr. Electr. Insul.*, 2019, **26**, 1204–1210.
- 37 N. Shi and R. Ramprasad, *IEEE Trans. Dielectr. Electr. Insul.*, 2008, **15**, 170–177.
- 38 M. Sato, A. Kumada, K. Hidaka, T. Hirano and F. Sato, *IEEE Trans. Dielectr. Electr. Insul.*, 2016, **23**, 3045–3052.
- 39 M. Sato, A. Kumada, K. Hidaka, T. Hirano and F. Sato, *IEEE Trans. Dielectr. Electr. Insul.*, 2016, **23**, 2978–2984.

- 40 M. Sato, A. Kumada and K. Hidaka, *J. Appl. Phys.*, 2018, **124**, 225104.
- 41 M. Sato, A. Kumada, K. Hidaka, T. Hirano and F. Sato, *Appl. Phys. Lett.*, 2017, **110**, 092903.
- 42 R. A. Marcus, *Rev. Mod. Phys.*, 1993, **65**, 599.
- 43 E. F. Valeev, V. Coropceanu, D. A. da Silva Filho, S. Salman and J.-L. Brédas, *J. Am. Chem. Soc.*, 2006, **128**, 9882–9886.
- 44 A. A. Voityuk and N. Rösch, *J. Chem. Phys.*, 2002, **117**, 5607–5616.
- 45 R. J. Cave and M. D. Newton, *J. Chem. Phys.*, 1997, **106**, 9213–9226.
- 46 A. A. Voityuk, *J. Chem. Phys.*, 2005, **123**, 034903.
- 47 S. F. Nelsen, S. C. Blackstock and Y. Kim, *J. Am. Chem. Soc.*, 1987, **109**, 677–682.
- 48 Q. Wu and T. V. Voorhis, *J. Phys. Chem. A*, 2006, **110**, 9212–9218.
- 49 M. Sato, A. Kumada and K. Hidaka, *Phys. Chem. Chem. Phys.*, 2019, **21**, 1812–1819.
- 50 P. J. Stephens, F. Devlin, C. Chabalowski and M. J. Frisch, *J. Phys. Chem.*, 1994, **98**, 11623–11627.
- 51 T. Lu and F. Chen, *J. Mol. Model.*, 2013, **19**, 5387–5395.
- 52 G. A. Petersson, A. Bennett, T. G. Tensfeldt, M. A. Al-Laham, W. A. Shirley and J. Mantzaris, *J. Chem. Phys.*, 1988, **89**, 2193–2218.
- 53 M. Sato, A. Kumada and K. Hidaka, *IEEE Trans. Dielectr. Electr. Insul.*, 2017, **24**, 574–582.
- 54 S. Serra, E. Tosatti, S. Iarlori, S. Scandolo and G. Santoro, *Phys. Rev. B: Condens. Matter Mater. Phys.*, 2000, **62**, 4389.
- 55 W. Wang, T. Takada, Y. Tanaka and S. Li, *IEEE Trans. Dielectr. Electr. Insul.*, 2017, **24**, 2599–2606.
- 56 L. Wang, Q. Li, Z. Shuai, L. Chen and Q. Shi, *Phys. Chem. Chem. Phys.*, 2010, **12**, 3309–3314.